Oxygen Doping Cooperated with Co-N-Fe Dual-Catalytic Sites: Synergistic Mechanism for Catalytic Water Purification within Nanoconfined Membrane

Ziwei Wang, Zhigang Yi, Lok Wing Wong, Xiang Tang, Hou Wang, Han Wang, Chengyun Zhou, Yangzhuo He, Weiping Xiong, Guangfu Wang, Guangming Zeng,* Jiong Zhao,* and Piao Xu*

Atom-site catalysts, especially for graphitic carbon nitride-based catalysts, represents one of the most promising candidates in catalysis membrane for water decontamination. However, unravelling the intricate relationships between synthesis-structure–properties remains a great challenge. This study addresses the impacts of coordination environment and structure units of metal central sites based on Mantel test, correlation analysis, and evolution of metal central sites. An optimized unconventional oxygen doping cooperated with Co-N-Fe dual-sites (OCN Co/Fe) exhibits synergistic mechanism for efficient peroxymonosulfate activation, which benefits from a significant increase in charge density at the active sites and the regulation in the natural population of orbitals, leading to selective generation of $SO_4^{\bullet-}$. Building upon these findings, the OCN-Co/Fe/PVDF composite membrane demonstrates a 33 min^{-1} ciprofloxacin (CIP) rejection efficiency and maintains over 96% CIP removal efficiency (over 24 h) with an average permeance of 130.95 L m^{-2} h^{-1}. This work offers a fundamental guide for elucidating the definitive origin of catalytic performance in advance oxidation process to facilitate the rational design of separation catalysis membrane with improved performance and enhanced stability.

1. Introduction

The growing global water scarcity underscores the need for sustainable wastewater treatment solutions that emphasize reusability, recyclability, and scalability.[1] Advanced oxidation processes (AOPs), particularly those based on peroxymonosulfate (PMS) activation, have emerged as a promising avenue for the rapid and efficient decomposition of organic pollutants through both radical and non-radical mechanisms.[2] Although existing catalysts exhibit high catalytic activity and stability, they remain inadequate in accurately identifying the active sites and selectively generating active species.

Atom-site catalysts have ascended as a forefront platform for tailoring the local coordination environment, thereby elucidating the intricate relationship between structural configurations and catalytic

Z. Wang, Z. Yi, H. Wang, C. Zhou, Y. He, W. Xiong, G. Wang, G. Zeng, P. Xu
College of Environmental Science and Engineering
Hunan University and Key Laboratory of Environmental Biology and Pollution Control (Ministry of Education)
Hunan University
Changsha 410082, P. R. China
E-mail: zgming@hnu.edu.cn; piaoxu@hnu.edu.cn
Z. Wang, L. W. Wong, J. Zhao
Department of Applied Physics
The Hong Kong Polytechnic University
Kowloon 999077, China
E-mail: jiongzhao@polyu.edu.hk

X. Tang
Fujian Provincial Key Laboratory of Soil Environmental Health and Regulation
College of Resources and Environment
Fujian Agriculture and Forestry University
Fuzhou 350002, P. R. China
H. Wang
School of Metallurgy and Environment
Central South University
Changsha, Hunan 410083, China

**ADVANCED
SCIENCE NEWS**

www.advancedsciencenews.com

**ADVANCED
MATERIALS**

www.advmat.de

properties.[3] In 2018, Zhang and Liu further proposed the single cobalt atoms as active sites for Fenton-like catalysis, contributing to a profound understanding of PMS-based AOPs by atom-site catalysts.[4] After that, more and more single-atom-site catalysts have been developed in recent years.[5] Strong interaction between support and metal atom sites usually serves as a pivotal conduit for precisely modulating the electronic configurations of center metal atoms, thus improving catalytic performance.[6] For example, researcher found that the substitution of C or N atoms with other nonmetal heteroatoms (e.g., B,[7] O,[8] S[9]) lead to an increase in available binding sites, which effectually modulated the local coordination environment. Meanwhile, the hetero-single atom catalysts comprising two different metal single-atom sites or dual metal atoms in the isolated active sites were designed to synergistically enhance catalytic activity.[10] Theoretically, the interaction of dual-atom site leads to a polarization of the charge distribution and elevate their electronic states toward the Fermi level, thereby improving the catalytic performance and regulating the reaction molecules/intermediates adsorption capacity toward selective generation of active species.[11] For instance, Zhao and Yin investigated the catalytic potential of bimetallic Fe–Co electrocatalysts, revealing an extraordinary performance in the production of ammonia.[12] Conspicuously, heteroatom dopants cooperated with dual-atom metal sites not only optimize the electronic properties but also bridge adsorption sites to regulate the adsorption configuration of reactant molecules.[13] However, the synergistic mechanism between heteroatom doped support and dual-atom metal sites on PMS activation have scarcely been explored.

Due to nontoxicity and eco-friendliness, graphitic carbon nitride (g-C_3N_4)-based atom-site catalysts sparked interest for their potential in the treatment of wastewater.[14] The micropores of g-C_3N_4 serve as ideal binding sites for anchoring metals due to the presence of sp^2 N atoms in the unique tri-s-triazine motif.[15] But its tunable structure of binding sites poses a complex challenge in identifying the active site and pyrolysis polymerization presents obstacles in achieving controllable synthesis.[15,16] The relationships between synthesis-structure-properties in g-C_3N_4-based atom-site catalysts remain largely unclear, yet novel strategies such as incorporating metal–support interaction and dual-atomic effect into the coordination environment have demonstrated to achieve highly catalytic activity, highlighting their potential contribution to definitively establish the origin of catalytic performance.

In this study, we synthesized an array of g-C_3N_4-based atom-site catalysts to delineate the unified guiding principles that govern the catalytic performance, employing statistical techniques like the Mantel test and correlation analysis for a comprehensive evaluation of the synthesis- structure-catalytic activity relationship. Moreover, Extended x-ray absorption fine structure (EXAFS), electron energy loss spectroscopy (EELS) and theoretical calculation were conducted to study the atomic structure, focusing on the influence of dual-atomic orbital coupling effects on catalytic activity and selectivity. Strikingly, the utilization of separation catalysis membrane (SM) represents a promising approach for the decontamination of water, in contrast to conventional methods such as heterogeneous Fenton-like reaction and pristine membrane filtration.[17] The proposed configuration enhances mass transfer from the site of active species generation to

the targeted pollutants, thereby effectively mitigating issues related to catalyst fouling and active species quenching.[17b,18] Consequently, we integrated the optimized OCN-Co/Fe catalysts onto polyvinylidene fluoride (PVDF) membranes within microreactors, facilitating a continuous flow reaction process characterized by exceptional activity and stability.

2. Results and Discussion

2.1. Design of g-C_3N_4-Based Atom-Site Catalysts

Based on previous investigation in our group, our design of g-C_3N_4-based atom-site catalysts for PMS activation is guided by the following principles (**Figure 1a**): 1) a N, O dual coordination structure can be introduced to the first shell of isolated metal atoms to stabilize metal atoms and modulate the oxidized states of metal atoms;[19] 2) the second metal atoms may be incorporated in the central active sites for further synergistically modulating the electronic structure of metal atoms, thus to decrease the barriers of substeps and accelerate the reaction rate,[12,16] 3) morphology control with high porosity and surface area are beneficial to anchor metal atoms and provide accessible possibility to the PMS.[20] Finally, advancing further from catalysts design to practical application, an urgent need for the area is large-scale production and device design of a membrane-based PMS microreactors.

Melamine and cyanuric acid were chosen as precursors for the support structure. Based on previous work, during polymerization, melamine and cyanuric acid interacted at the molecular level to introduce doping and functional groups.[8,21] Importantly, these doping or functional groups provide a stronger covalent metal–support interaction, thus efficiently anchoring metal atoms. Briefly, g-C_3N_4-based atom-site catalysts surrounded with cyano groups and N, O dual coordination structure were prepared. A series of OCN-Co catalysts with different metal loading and concentrations of functional groups were synthesized using the same ball-milling method (As shown in Table S1, Supporting Information, the number represents the concentration of metal precursor or carrier precursor). Under optimized experimental conditions, the OCN-Co, OCN-Fe, and OCN-Co/Fe were further prepared with different synthetic conditions, including different support, atmosphere (Ar) and acid washing. More importantly, this synthesis method facilitated the large-scale production of the catalyst with yield of 14.07% (Figure S1, Supporting Information). All catalysts were characterized by organic elemental analyzers (OEA), inductively coupled plasma-mass spectrometry (ICP-MS), X-ray diffractometer (XRD), and Brunner−Emmet−Teller (BET). The structural information of catalysts was further revealed by X-ray photoelectron spectroscopy (XPS) transmission electron microscope (TEM), and high-resolution TEM (HRTEM). More detailed experiment conditions and characterization results of each catalyst were listed in Supporting Information.

2.1.1. Modifications of the g-C_3N_4 Support

To investigate the variation of support, we performed BET, OEA, XRD, and Fourier transform infrared spectrometer (FT-IR) and

**ADVANCED
SCIENCE NEWS**

www.advancedsciencenews.com
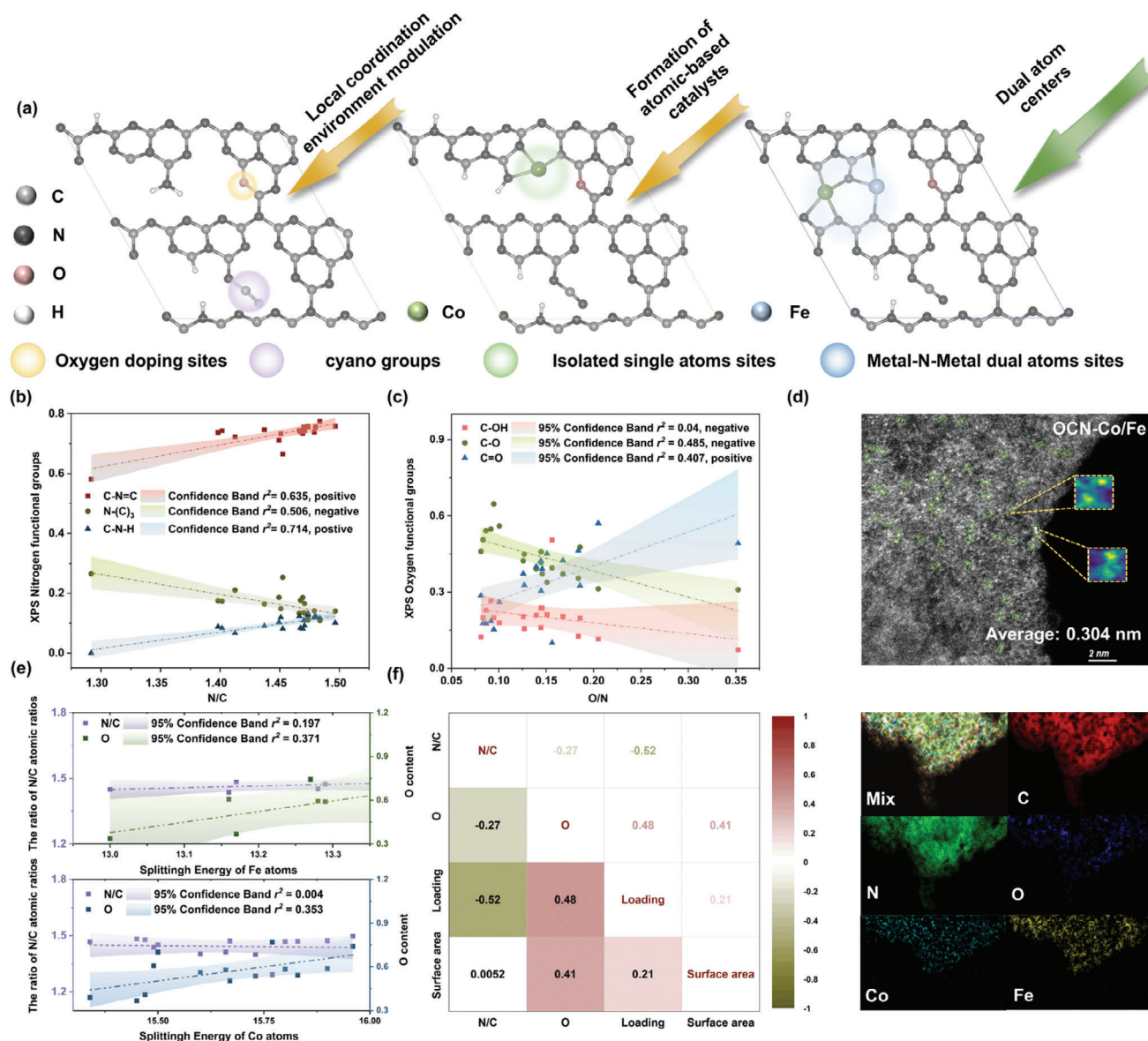
**ADVANCED
MATERIALS**

www.advmat.de

Figure 1. a) Illustration of catalyst design based on coordination environment optimization and electronic structure optimization, b) relationships between N/C atomic ratios and XPS nitrogen functional groups, c) relationships between O/N atomic ratios and XPS oxygen functional groups, d) HAADF STEM images of OCN-Co/Fe and statistical dual metal center spacing, and OCN-Co/Fe STEM- EELS mapping spectra, e) relationships between the oxidation states of Fe atoms and the ratio of N/C atomic and O content, relationships between the oxidation states of Co atoms and the ratio of N/C atomic and O content, f) correlation among surface area, N vacancies (N/C atomic ratios), oxygen content, loading of metal atoms based on *Spearman's* correlation coefficients.

XPS. In total, 21 kinds of g-C_3N_4 based catalysts were successfully synthesized, of which the loading of metal atoms and proportions of melamine/cyanuric acid must be considered to obtain crystalline g-C_3N_4 support. For instance, the support transitioned to amorphous N-doped carbon with Co atom loading at 30 wt.% (Figure S2a, Supporting Information). And the Co_3O_4@C was obtained by the calcination of cyanuric acid-based precursors (Figure S2b, Supporting Information). Except for Co_3O_4@C and OCN-Co-8, all the catalysts maintained the basic skeleton of carbon nitride, while an obvious variation could be found in the FT-IR spectra, emphasized by shaded regions

in Figure S3 (Supporting Information). The increases in the intensity of peaks at 2177 cm^{-1} corresponded to the cyano groups (—C≡N).[22] Furthermore, the obvious decreased N/C atomic ratios (from 1.502 to 1.469) and increased O contents (from 0.663 to 0.681) based on OEA analysis suggested that surface N defects and oxygen doping were incorporated into catalysts (Table S2, Supporting Information).[21,22] To investigate the formation of defect sites, we correlated the N/C atomic ratios with functional groups in XPS spectrum (Figures S5–S9 and Table S3, Supporting Information). Specifically, as shown in Figure 1b, a positive correlation with high coefficients ($r^2 = 0.635$) was

observed between N/C atomic ratios and C—N≡C functional groups. A similar phenomenon was also observed between N/C atomic ratios and C—N—H groups (positive, $r^2 = 0.714$). It should be noted that the introduction of cyano groups cannot alter the N loss in the framework. Considering the high coefficients between N/C atomic ratios and C—N—H groups could be ascribed to the formation of cyano groups, our finding emphasized that nitrogen vacancies were mainly introduced into C—N≡C functional groups of the support. Interestingly, we further focused on the correlations between various O functional groups with O/N atomic ratios (Figure 1c). The results revealed that increased tendency of concentrations of C=O groups was highly positive consistent with that of O/N atomic ratios ($r^2 = 0.407$), indicating partial nitrogen vacancies would be replaced by oxygen to eventually form oxygen doping sites.[23] Therefore, in our following analysis, oxygen doping sites would be associated with the concentration of oxygen atoms, while the introduction of cyano groups is negatively correlated with the N/C ratios. The proposed support structure was illustrated in Figure 1a.

2.1.2. The Structure of the Metal Active Centers

To identify the atomic(crystal) structures of catalysts, we performed multiple microscopic techniques such as XRD, TEM, HRTEM and aberration-corrected annular dark field scanning transmission electron microscopy (HAADF-STEM). As shown in Figures S10 and S11 (Supporting Information), HRTEM images indicated the metal oxides obtained over the calcination of cyanuric acid or melamine precursors. The absence of characteristic peaks of CoO in XRD patterns was possibly ascribed to the low loading and crystallinity. After the mixture of melamine/cyanuric acid, the construction of metal-atom sites had developed as no nanoparticles were observable (Figures S12–S14, Supporting Information). As shown in Figure 1d and Figure S15 (Supporting Information), the metal atom-sites in the optimized catalysts (two monometallic Co, Fe catalyst and a bimetallic Co/Fe catalyst, denoted by OCN-Co, OCN-Fe, OCN-Co/Fe) were atomically dispersed as evidenced by HAADF-STEM. Additionally, the uniform distribution of Co and Fe atomic sites was demonstrated by EELS-STEM mapping image. The calculated average spacing between dual atoms (more than 50 atom pairs) based on STEM images was ≈0.306 nm (Figure S16a, Supporting Information).

Subsequently, to explore the chemical states of metal atoms, the valence state of Co and Fe species were determined by XPS, in which the Co resembled +2 while the Fe was between +2 and +3. We further used the energy of spin–orbit splitting to present the charge density state of metal atoms (Figures S5–S9, Supporting Information).[19b] Thus, lower charge density state of metal atoms due to lower spin–orbit splitting has suggested the highly oxidized atom centers. To elucidate the influence of changes in local coordination structures on the oxidation states of metal atoms, we performed a linear regression analysis between the oxidation states of metal atoms (the energy of spin–orbit splitting), cyano groups and oxygen doping. As shown in Figure 1e, the results demonstrated a positive correlation between metal centers (Co, Fe) and O content ($r^2 = 0.353$ and 0.371, respectively), suggest-

ing the blue shift of spin–orbit splitting energy after the introduction of O atoms.[24] This phenomenon was consistent with the observation that Co 2p signals shifts slightly to a lower binding energy.[25] In contrast, cyano groups only showed a negligible impact on the oxidation states ($r^2 = 0.004$ and 0.194, respectively). Oxygen doping had a stronger negative effect on the oxidation state of the active metal center than the cyano functional group, indicating that the oxygen doping sites might be closer to the active metal center in the coordination shell. The proposed structure of metal atoms anchored on support were illustrated in Figure 1a.

To explore the overall variability in community catalysts, we tackled the challenge of disentangling the correlation among surface area, cyano groups (represented as N/C atomic ratios), oxygen doping (represented as O content), loading of metal atoms (Figure 1f; Table S2, Supporting Information). The results revealed that oxygen content was moderately relevance with surface area and loading of metal atoms ($0.3 \leq R < 0.5$). Simultaneously, a negative correlation with stronger coefficients ($R = 0.52$) was observed between loading of metal atoms and N/C atomic ratios. Our finding emphasized the importance to generate cyano groups and oxygen doping during synthetic process. These functional groups and doped atoms might provide abundant surface anchoring sites for metal atoms, thus reflecting the associated interactions adapted to the observed increase in the loading of metal atoms.[16] In addition, more surface area has been suggested to increase the spatial location between metal atoms, thus further in favor of atom-site catalysts.[8] Given the importance of size parameters, we tested the atomic structures of catalysts using cobalt-based catalysts as examples, where the isolated metal atoms tended to aggregate with the increase of metal loading and finally formed clusters in the support (Figure S16b, Supporting Information). The independent model associations of metal precursors ratio with surface area presented the strong negative correlation ($r^2 = 0.91$), indicating the formed clusters might occupy the pores structure in the support (Figure S17, Supporting Information).

2.2. Evaluation of Catalytic Activities

Following the synthesis of 21 kinds of distinct g-C$_3$N$_4$-based catalysts, we evaluated their performance through PMS-based advanced oxidation processes, employing ciprofloxacin (CIP) as the model pollutant. To obtain the optimized experiment conditions, we first recorded the reaction rates (k_{obs}) of based on the removal efficiency of CIP within 20 min via PMS activation and combined these data based on normalization of metal contents (k_{mass}), surface area ($k_{surface area}$) (**Figure 2a,b**; Figure S18 and Table S4, Supporting Information). The advantages of air-calcined dual-atom-site catalysts (OCN-Co/Fe) over other catalysts were prominently observed: It showed the highest removal efficiency with CIP up to 100% within 6 min. The k_{mass} and $k_{surface area}$ of OCN-Co/Fe were up to 3.80×10^5 min^{-1} mol^{-1} and 0.0105 g (m^2)$^{-1}$ min^{-1}, respectively, which were far greater than those of other catalysts. Notably, the k_{mass} after acid washing process (OCN-Co/Fe-W) was similar to the OCN-Co/Fe, which indicated the dominated atomic active sites that actively participated in catalytic process in OCN-Co/Fe.
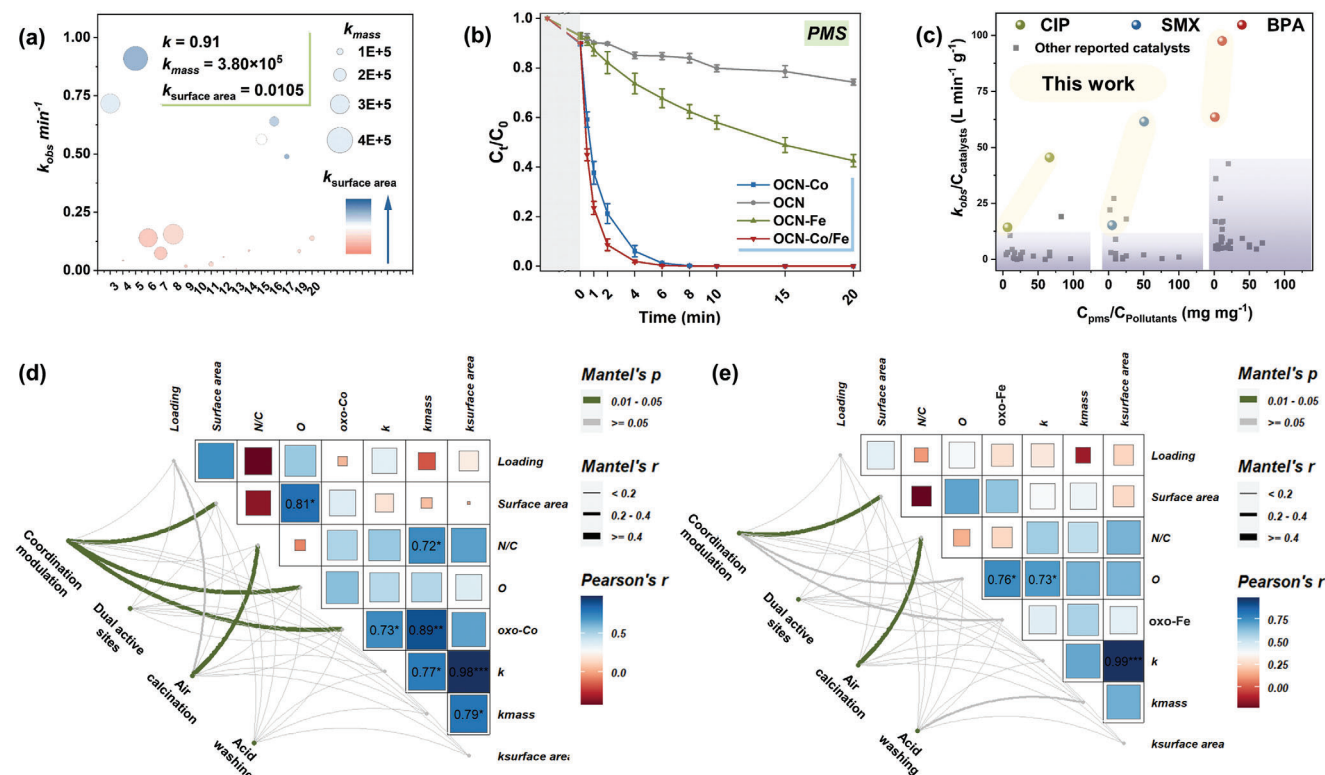
Figure 2. a) Degradation performance of CIP in different catalysts activated PMS systems corresponding degradation rate including normalized k value by per mole M atom and surface area, b) degradation performance of CIP in OCN, OCN-Co, OCN-Fe, OCN-Co/Fe activated PMS systems, c) comparisons of catalytic efficiency of OCN-Co/Fe with those of reported materials, dose-normalized rate constant (k) magnitude versus PMS/pollutant concentration ratios, d) pairwise comparisons of synthesis-structure-properties for cobalt-based catalyst are shown, with a color gradient denoting Spearman's correlation coefficient. Synthesis concept based on the four principles (coordination modulation (ratio of cyanuric acid and metal source in precursor), dual active sites, air calcination, acid washing) was related to each structure-properties factor by partial (geographic distance–corrected) Mantel tests. Edge width corresponds to the Mantel's r statistic for the corresponding distance correlations, and edge color denotes the statistical significance. e) Pairwise comparisons of synthesis–structure–properties for iron-based catalyst are shown, with a color gradient denoting Spearman's correlation coefficient. Synthesis concept based on the four principles (coordination modulation (ratio of cyanuric acid and metal source in precursor), dual active sites, air calcination, acid washing) was related to each structure-properties factor by partial (geographic distance-corrected) Mantel tests. Edge width corresponds to the Mantel's r statistic for the corresponding distance correlations, and edge color denotes the statistical significance. Reaction conditions: [CIP] = 5 mg L^{-1}, [PMS] = 1 mM, catalysts = 0.02 g L^{-1}, T = 298 K, initial solution pH 6.5.

Considering the outperformed performance, we chose OCN-Co/Fe for more detailed study. The broad-spectrum removal experiment suggested that carbamazepine, atrazine, bisphenol A, sulfamethoxazole and phenol were also full decomposed within 6 min (Figure S19a, Supporting Information). These catalyst-dose-normalized rate constants were monitored as a function of PMS/pollutants concentration ratios,[26] revealing the remarkable catalytic activity of OCN-Co/Fe compared to previously reported materials (Figure 2c; Table S5, Supporting Information). Repeated experiments showed that OCN-Co/Fe still maintained over 99.9% removal efficiency after 5 cycles and the reused catalysts displayed good crystal structure, morphology and isolated metal atoms (Figures S19c and S20, Supporting Information). Furthermore, only a slight suppression of the catalysis was observed in various water systems (tap water, river water and deionized water with humic acid), indicating the excellent stability of OCN-Co/Fe (Figure S19b, Supporting Information).

2.3. Strong Interaction Between Oxygen Doped Support and Metal Atoms

The good performance for PMS activation and promising stability motivated us to definitively demonstrate the origin of catalytic activities and further explore the strong interaction between the atomically dispersed atoms and support. Each change point on support provides some indication about the improvement of catalytic performance (as we summarized in design of g-C$_3$N$_4$-based atom-site catalysts), but it is crucial to identify the factors that govern the intrinsic catalytic activity. Thus, we firstly investigated the potential correlations between the effect factors and k_{obs} using color gradient denoting Spearman's correlation coefficients (Figure 2d,e). The strength of these associations was rigorously tested in cobalt-based catalysts (Figure 2d), revealing significantly strong positive correlations between the oxidation states of metal atoms, k_{obs} and k_{mass} (0.73 and 0.89, respectively). Another important result of the Spearman's correlation coefficients in

ADVANCED
SCIENCE NEWS

www.advancedsciencenews.com

ADVANCED
MATERIALS

www.advmat.de

iron-based catalysts was that a positive significant correlation between O content and k_{obs} as well as oxidation states were observed (0.76 and 0.73, respectively), indicating the oxidation states of active sites played the critical roles in catalytic process (Figure 2e). It was suggested that the oxidation states of active sites were directly related with the intrinsic activity. Usually, the blue shift of oxidation states is intimately related to the increase of charge density state and the downshift of the d-band center, attributing to a stronger electronic-donating ability.

Because of the complex changes into structure resulting from synthetic conditions and introduction of bimetallic metal atoms, we subsequently attempted to discern the roles of individual deterministic factors in catalysts structure. Consequently, we employed the partial Mantel test to correlate divergences in synthetic conditions with effect factors and the catalysts' catalytic performance (Figure 2d,e).[27] Overall, the Mantel test demonstrated that coordination modulation (ratio of cyanuric acid and metal source in precursor) was strong related with surface area, O content and oxidation states of metal atoms for cobalt-based catalysts. The results further revealed that the formation of cyano groups was found related to air calcination. Air calcination could efficiently decrease the concentration of cyano groups, thereby exhibiting higher catalytic efficiency. Although acid washing is a widely used method for atom-site catalysts synthesis, it showed neglected impacts in our system, which may be ascribed to the direct formation of atom-site catalysts via oxygen doping strategy.

Taken together, benefitting from strong interaction between oxygen doped support and metal active centers, a rational design strategy for synthetic conditions and subsequent modulation of chemical states of active metal sites through the modulation of local coordination environment may, at least for our system, represented a mechanism for the enhancement of catalytic performance. Spearman's correlation coefficient indicated k_{obs} and k_{mass} were highly positive related with the oxidation states of metal atoms, indicating an electron transfer-dependence for PMS-based AOPs. The Mantel test analysis revealed that the incorporation of oxygen-containing precursors predominantly influenced the catalysts' larger surface area, increased oxygen content, and the blue shift in oxidation states of metal atoms. However, the Mantel test analysis yielded inconclusive results in substantiating a significant dual-atomic synergistic effect, potentially attributable to the lack of characterizations at atomic level to explore the variations at electronic structure.

2.4. Dual Atoms Coupling Effect

The coupling effect of dual atoms was elucidated through XANES and EELS analyses, corroborated by evaluations of catalytic performance and active species generation. XANES spectroscopy at the Co K-edge and Fe K-edge was utilized to delineate the coordination environments within OCN-Co, OCN-Fe, and OCN-Co/Fe catalysts. In OCN-Co/Fe, the Co active sites demonstrated a shift in the absorption edge toward lower energy, with a concurrent broadening of the white line peak, signifying a depressed oxidation state of the metal active centers (**Figure 3a**).[28] However, The Fe active sites in OCN-Co/Fe exhibited an opposite shift of the absorption edge. Correspondingly, the Co—N(O) and Fe—N(O) bonds in the k^3-weighted K edge EXAFS spectrum of OCN-Co,

OCN-Fe, and OCN-Co/Fe showed an obvious shift, in which the characteristic peak of Fe displayed higher-R shift (from 1.48 to 1.53 Å) and the characteristic peak of Co displayed lower-R shift (from 1.60 to 1.54 Å, Figure 3b). These results indicated may exist a rearrangement in their local coordination environment as reflected by the XANES results.[11b,29]

We further fitted the EXAFs spectra to deduce the coordination number (CN) and geometric configuration of the active metal centers. From the supplementary Table S6 and Figure S21 (Supporting Information), the fitting results indicated that Co species in OCN-Co and Fe species in OCN-Fe exhibited one coordinating interaction, at 2.10 ± 0.06 Å with CN of 5.37 ± 0.64 and 1.99 ± 0.01 Å with CN of 5.91 ± 0.90, corresponding to Co—N(O) bonds and Fe—N(O) bonds, respectively. Note that for OCN-Fe, a Fe-Fe path at 2.46 Å was observed, indicating the formation of Fe-based clusters. Compared with that of OCN-Fe, the bond length of a Co-N-Fe peak in both the Fe and Co species of OCN-Co/Fe was 2.58 Å, longer than that for metal-metal path.[12,30] Additionally, the Fe species in OCN-Co/Fe displayed similar coordinating interaction, at 1.99 ± 0.10 Å with CN of 4.83 ± 0.55. When isolated cobalt atoms cooperated with iron atoms, Co—N(O) bonds showed characteristic peaks originating from five Co—N coordination with asymmetric bond lengths of 1.99 ± 0.02 and 2.10 ± 0.03 Å, inferring a significant change in the coordination structure.[31] The wavelet transform results of the K-edge EXAFS oscillations were used to support the EXAFS analysis (Figure 3a). The Fe species in OCN-Fe and OCN-Co/Fe exhibited the WT maximum at ≈5.3 Å^{-1} corresponding to Fe—N(O) bonds. In contrast, the WT maximum of Co species in OCN-Co/Fe shifted from 5.2 to 4.75 Å^{-1}. All the above data suggested that, as cobalt atoms coupled with Fe atoms in OCN framework, Co-N-Fe dual-atom sites were formed (The proposed structure was illustrated in Figure 1a; more details are listed in the Figures S22–S25, Supporting Information).

These rearrangement in coordination shells may lead to a greater change in the electronic structure of dual metal atom centers.[32] EELS using inelastically scattered electrons could provide direct evidence of these changes. As shown in Figure 3c, the EELS signal detected the Fe and Co L-edge at 711 and 781 eV, which unequivocally demonstrated the dual atoms presence. The signal intensity from Co/Fe dual atomic sites, at lower loadings, surpassed that of monometallic counterparts, implying enhanced electron beam irradiation tolerance attributable to a synergistic effect.[33] Furthermore, the Co L-edge EELS spectra collected after coupling with Fe atoms exhibited an L_3/L_2 ratio of ≈4.22, higher than that of OCN-Co. The measured L_3/L_2 ratio of Fe species in OCN-Co/Fe exhibited the opposite trend, indicating the occurrence of bimetallic synergy effects that led to a rearrangement in valence states of dual metal atoms.[34]

To investigate the changes in performance and stability arising from alterations in the electronic structure of dual active centers, we utilized the slope of $k_{surface\ area}$ versus the PMS oxidant to compare the intrinsic activity of OCN-Co and OCN-Co/Fe (Figure 3d). The slope for OCN-Co/Fe increased from 0.006 to 0.008, indicating that the coupling effect of dual atom sites in OCN-Co/Fe catalysts improved oxidant activation over the catalyst surface.[35] Also, the degradation of CIP was performed on OCN-Co and OCN-Co/Fe under different pH conditions and in the presence of various inorganic anions. Both of catalysts indicated the
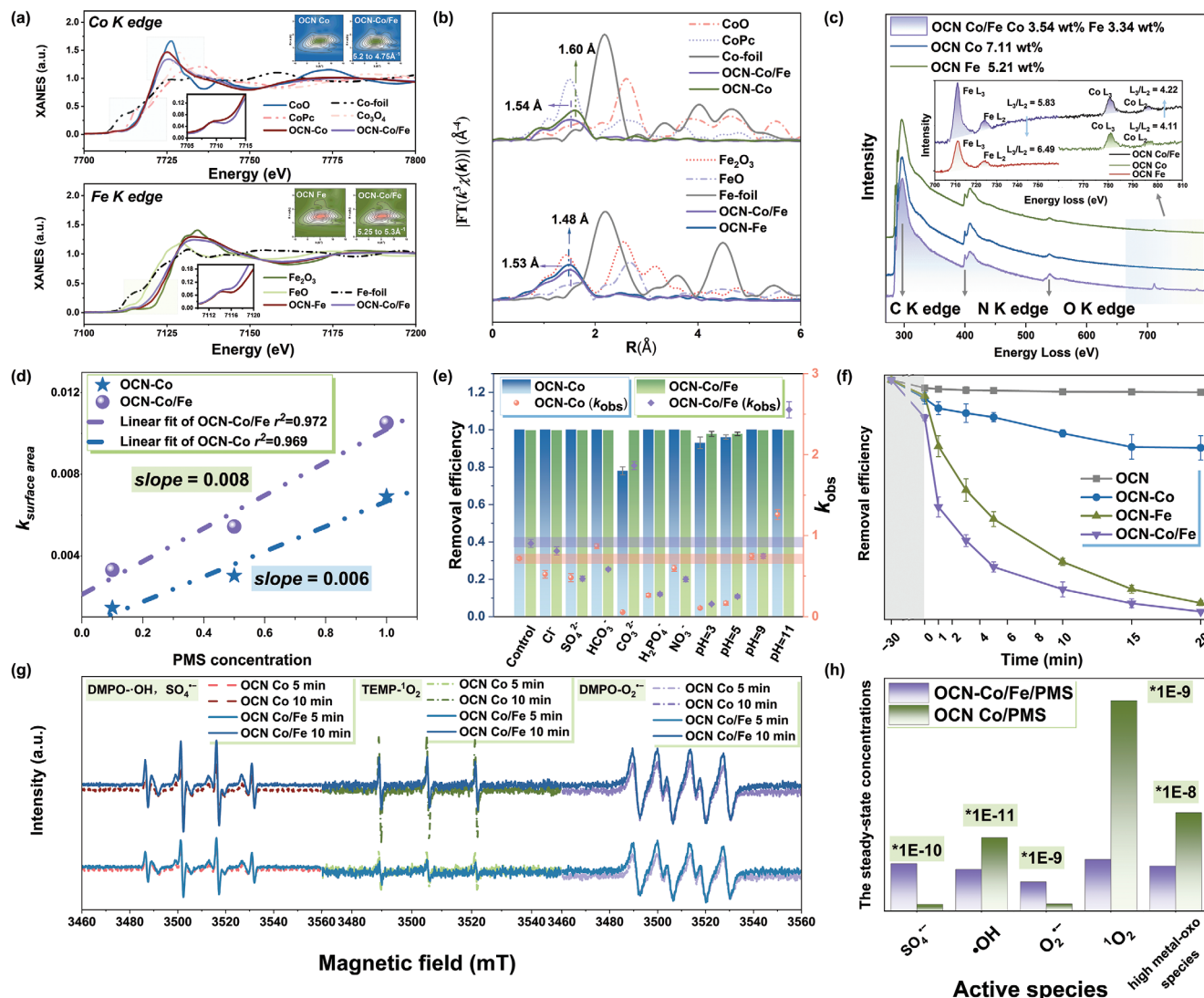
ADVANCED
SCIENCE NEWS

www.advancedsciencenews.com

ADVANCED
MATERIALS

www.advmat.de

Figure 3. a) Co R-space EXAFS spectra for Co foil, CoO, OCN-Co, and OCN-Co/Fe and Fe R-space EXAFS spectra for Co foil, CoO, OCN-Fe, and OCN-Co/Fe, b) Co K-edge XANES profiles for Co foil, CoO, Co$_3$O$_4$, OCN-Co, and OCN-Co/Fe; Fe K-edge XANES profiles for Fe foil, FeO, Fe$_2$O$_3$, OCN-Fe, and OCN-Co/Fe, and corresponding WT-EXAFS spectra for OCN-Co, OCN-Fe, and OCN-Co/Fe, c) three EELS spectrums exhibit a trace of Fe and Co L-edge for OCN-Co, OCN-Fe and OCN-Co/Fe, d) degradation performance of CIP in OCN-Co and OCN-Co/Fe activated PMS systems for the effect of initial PMS concentrations on k value by surface area, d) removal efficiency and k value in OCN-Co and OCN-Co/Fe activated PMS system in different pH and the presence of different ions, e) degradation performance of CIP in OCN, OCN-Co, OCN-Fe, OCN-Co/Fe activated H$_2$O$_2$ systems, f) degradation performance of CIP in OCN, OCN-Co, OCN-Fe, OCN-Co/Fe activated H$_2$O$_2$ systems, g) EPR spectra of •OH, SO$_4$•$^-$, O$_2$•$^-$, and ^{1}O$_2$, h)the steady–state concentrations of various active species in OCN-Co and OCN-Co/Fe activated PMS systems. Reaction conditions: [CIP] = 5 mg L^{-1}, [PMS] = 1 mM, [H$_2$O$_2$] = 20 mM, catalysts = 0.02 g L^{-1}, T = 298 K, initial solution pH 6.5, [Cl$^-$, CO$_3^{2-}$, HCO$_3^-$, SO$_4^{2-}$, H$_2$PO$_4^-$] = 5 mM.

exceptional stability but the reaction rate was slightly affected, in which OCN-Co/Fe exhibited stronger tolerance (Figure 3e). The synergistic effect of bimetallic active sites was further proved by H$_2$O$_2$-based AOPs, compared to OCN-Co and OCN-Fe, the catalytic activity of OCN-Co/Fe is significantly enhanced with CIP removal efficiency up to 100% within 20 min (Figure 3f).

To explore the changes in the reactive species arising from alterations in the electronic structure, electron paramagnetic resonance (EPR) spectroscopy and scavenging experiments were used to explore the roles of •OH, SO$_4$•$^-$, ^{1}O$_2$, O$_2$•$^-$, and high-metal-oxo species (more details are given in Supporting Information). As shown in Figure 3g, the EPR spectrum of OCN/Co

and OCN-Co/Fe exhibited the characteristic peaks of DMPO–•OH (peak intensity ratio 1:2:2:1), DMPO–SO$_4$•$^-$(peak intensity ratio 1:1:1:1:1:1), DMPO–O$_2$•$^-$(peak intensity ratio 1:1:1:1) and TEMP–^{1}O$_2$ (peak intensity ratio 1:1:1), indicating the formation of various reactive species. We also found that PMS activation was preferred to ^{1}O$_2$ production for OCN-Co, whereas OCN-Fe/Co showed enhanced DMPO–•OH and DMPO–SO$_4$•$^-$ signals. These results were further semi quantified by the scavenging experiments. In OCN-Co/Fe/PMS system, the inhibition values of the reactive species were followed as: O$_2$•$^-$ > •OH > ^{1}O$_2$ > SO$_4$•$^-$; while in OCN-Co/PMS system, the inhibition values of these were followed as: O$_2$•$^-$ > SO$_4$•$^-$ > •OH ≈ ^{1}O$_2$ (Figure S26,

ADVANCED
SCIENCE NEWS

www.advancedsciencenews.com

ADVANCED
MATERIALS

www.advmat.de

Supporting Information). Commonly, individual active species is sensitive to different functional groups of organic molecules, generating various degradation pathway.[36] The vibrations in the intermediates of the OCN-Co/PMS/CIP and OCN-Co/Fe/PMS CIP systems, as determined by liquid chromatography-tandem mass spectrometry (LC-MS) analysis, further proved the changes in produced active species (Figures S27–S30, Supporting Information). Thus, different probes were used to quantify the steady-state concentrations of $\bullet$OH, $SO_4^{\bullet-}$, $^1O_2$, $O_2^{\bullet-}$, and high-metal-oxo species.[37] As shown in Figure 3f, Figure S31 and Table S7 (Supporting Information), the steady–state concentrations of $SO_4^{\bullet-}$ for OCN-Co/Fe/PMS system was 1.74×10^{-10} M, which was 4.26 times higher than that of OCN-Co/PMS system (2.52×10^{-11} M). Furthermore, the steady-state concentrations of $^1O_2$ and high metal oxo for OCN-Co/Fe /PMS system was 1.89×10^{-9} and 1.65×10^{-8} M (Figure S32, Supporting Information), which was 0.245 and 0.458 times lower than that of OCN-Co/PMS system (7.69×10^{-9} and 3.6×10^{-8} M, respectively). In summary, the synergistic effect of dual atoms contributed to alterations in the coordination architecture and electronic structure of the metal centers, culminating in enhanced catalytic activity, stability, and selective generation of sulfate radicals.

2.5. Theoretical Calculations

Theoretical simulations, pivotal for elucidating atomic-level material characteristics, were executed to precisely investigate material properties. Given the comprehensive studies on the strong interactions between oxygen-doped carbon nitrogen frameworks and metal atoms, theoretical analyses were primarily aimed at demystifying the electronic delocalization facilitated by dual-atomic orbital interactions. Electrochemical assays confirmed the electron transfer from metal atoms to PMS, evidenced by **Figure** 4a and Figure S33 (Supporting Information). Then, the detailed electronic structures and a reactivity characterization were illustrated by the partial density of states (DOS) of Co 3d and Fe 3d orbitals as well as their d band centers.[38] As shown in Figure 4b, after the Co metal atoms were incorporated with Fe active sites, the d bands of metals were spin polarized due to d–d orbital coupling.[39] Within the OCN-Co/Fe framework, cobalt acted as an electron-deficient center, characterized by elevated 3d orbitals (e_d increase from -1.33 from -0.39, average), reducing the occupancy of metal-molecule antibonding states. In total, the distinctive electronic configuration endowed the dimer with a heightened capacity for electron transfer, thereby facilitating favorable interactions with PMS.[40]

The adsorption energy, electron transfer number, and O—O bond length elucidate the interaction dynamics between PMS and the catalysts. As shown in Figure 4c, both isolated cobalt and iron atoms preferentially adsorbed the O1 sites of PMS rather than O2 sites. While OCN-Co/Fe was inclined to simultaneously adsorb the O1 sites and O2 sites of PMS, which could be ascribed to the synthetic effect of dual atoms.[31,41] As a result, OCN-Co/Fe exhibited the highest adsorption energy (-2.98 eV) and a weaker O—O bond (1.47 Å). Bader charge analysis of confirmed a significant charge transfer to PMS* from Co-N-Fe dual atomic sites (2.16 electrons), which is significantly higher than the 0.82 electrons and 1.26 electrons for OCN-Co-PMS* and OCN-Fe-PMS*.

In the context of catalysis or redox reactions, this could imply that Co/Fe-PMS* might have a stronger electron-withdrawing or donating ability compared to OCN-Co-PMS* and OCN-Fe-PMS*, which may affect its catalytic activity or stability.

A paramount challenge in PMS activation lies in the selective generation of active species. Recently studies indicated that *O is the key intermediates toward high-metal-oxo species and $^1O_2$.[8,37a] The oxygen atom transfer reaction was identified by the selective production PMSO^{16}O^{18} via ^{18}O-isotope labeling experiments (Figure S34, Supporting Information).[42] Therefore, for comparison, we calculated the reaction pathway toward *O production (Figure 4d,e; Figure S35, Supporting Information). All of catalysts thermodynamically favor the free energy profiles of PMS → PMS*→ SO$_4$* and OH*. Subsequent reaction consists of the dissociation of SO$_4$* and the generation of *O intermediate. The d–d orbital hybridization of dual-metal atoms played a significant role in facilitating the dissociation of SO$_4$* while impeding the subsequent formation of *O. Specifically, In the dissociation of SO$_4$*, the increased energy barrier was lower on OCN-Co/Fe (0.06 eV) compared to OCN-Co (0.32 eV). Conversely, the free energy barrier for the formation of *O from 2OH* showed an increase from 0.74 eV (OCN-Co) to 1.02 eV (OCN-Co/Fe). Then, we introduced the crystal orbital Hamilton population (COHP) between the metal site and O atom (SO$_4$*), showing the strength of the oxygen bridge to metal sites.[43] The less positive -ICOHP means the weaker M—O bonds, thus favoring the formation of SO$_4^{\bullet-}$. As shown in Figure 4f, it is clear that interaction of SO$_4$* with metal active sites in OCN-Co/Fe decreased from 0.7 (OCN-Co/SO$_4$*) and 0.32 (OCN-Fe/SO$_4$*) to 0.02 and 0.05. Therefore, OCN-Co/Fe/PMS promoted SO$_4^{\bullet-}$ generation while hindering high-metal-oxo species and $^1O_2$ generation. This hypothesis is in agreement with the analysis of catalytic performance and electronic structure model, providing compelling evidence that the incorporation of oxygen atoms and the dual-atomic effect into the coordination environment confers advantages for the activation of PMS and selective production of active species.[11b,44]

In summary, incorporating additional oxygen atoms into the coordination shell of metal active sites not only stabilized these atoms but also modulated their oxidation states, thereby enhancing catalytic performance. Subsequently, the introduction of second metals in the central active sites allowed a rearrangement in their local coordination environment to form Co-N-Fe dual-atom site. The catalytic efficacy was superior in OCN-Co/Fe catalysts, which combined the oxygen doping sites and Co-N-Fe dual-atom site into the coordination environment, exhibiting the higher catalytic performance, oxidation utilization and stronger environmental tolerance. The DFT simulation supplemented our mechanistic insights into the dual atoms coupling effect regarding a stronger electron-donating ability (PMS*) and a weaker M—O bonds between the metal site and O atom (SO$_4$*), leading to the improvement in PMS-based AOPs performance and selective generation of SO$_4^{\bullet-}$ species.

2.6. Continuous Flowing Treatment

The remarkable catalytic activity and stability inspired the integration of PMS activation with membrane separation technologies at a device level. Catalytic lamellar membranes were
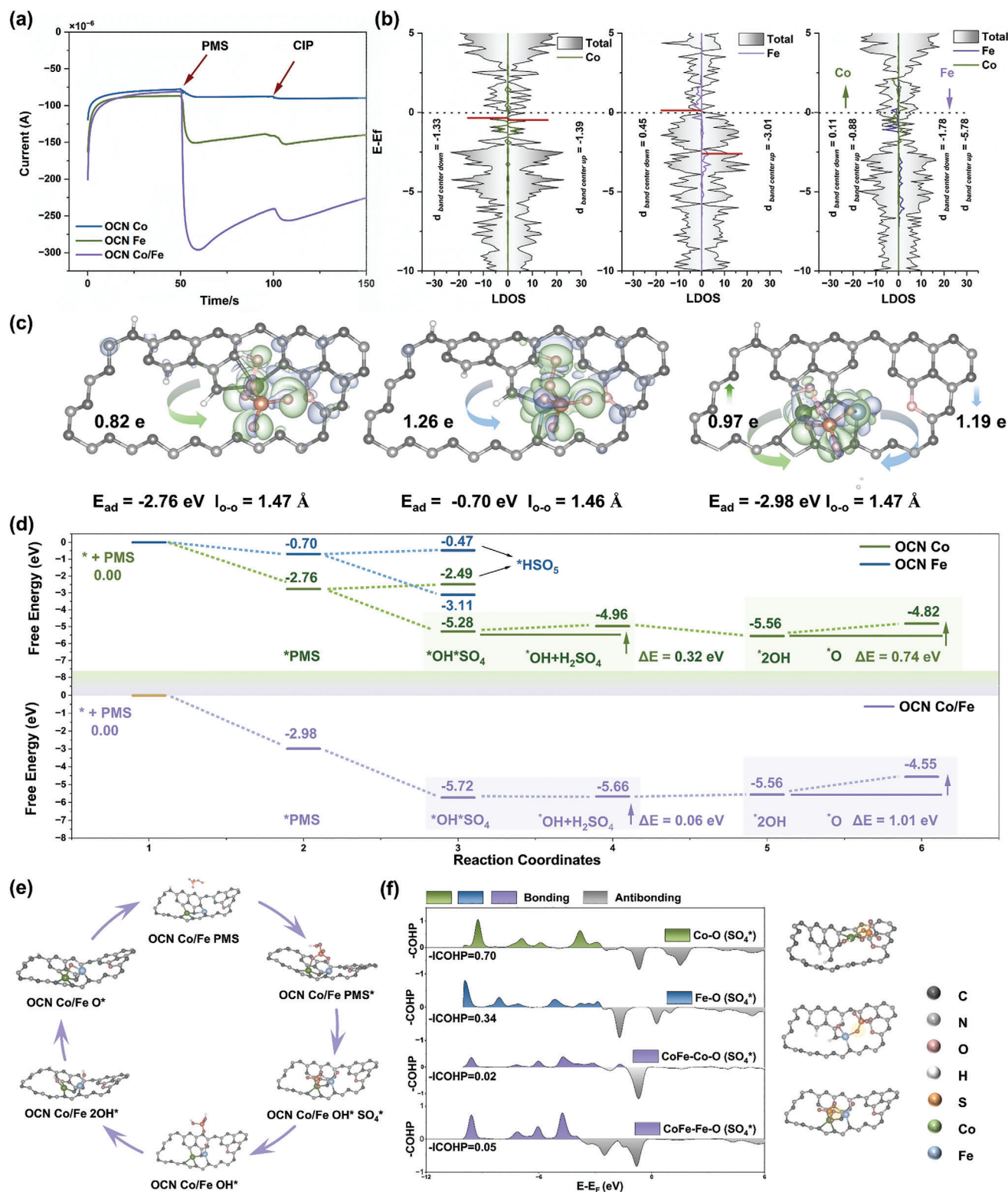
2404278 (8 of 13)

**ADVANCED
SCIENCE NEWS**

www.advancedsciencenews.com

**ADVANCED
MATERIALS**

www.advmat.de

Figure 4. a) Current versus time curves, b) projected DOS onto Co and Fe 3d orbitals of OCN-Co, OCN-Fe, and OCN- Co/Fe, and O 2p orbital of OCN-Co/PMS, OCN-Fe/PMS, and OCN- Co/Fe/PMS. The vertical solid lines are used to denote the d-band center, c) bader charge analysis of PMS on OCN-Co, OCN-Fe, and OCN- Co/Fe, d) the calculated potential energy diagrams for SO$_4$* and OH* moieties oxidation to O* on OCN-Co, OCN-Fe, and OCN- Co/Fe catalysts, e) the corresponding structures of reaction intermediates for proposed reaction process, f) projected crystal orbital Hamilton population (pCOHP) between the metal center and the oxygen adatom (SO$_4$*), and their corresponding structures.
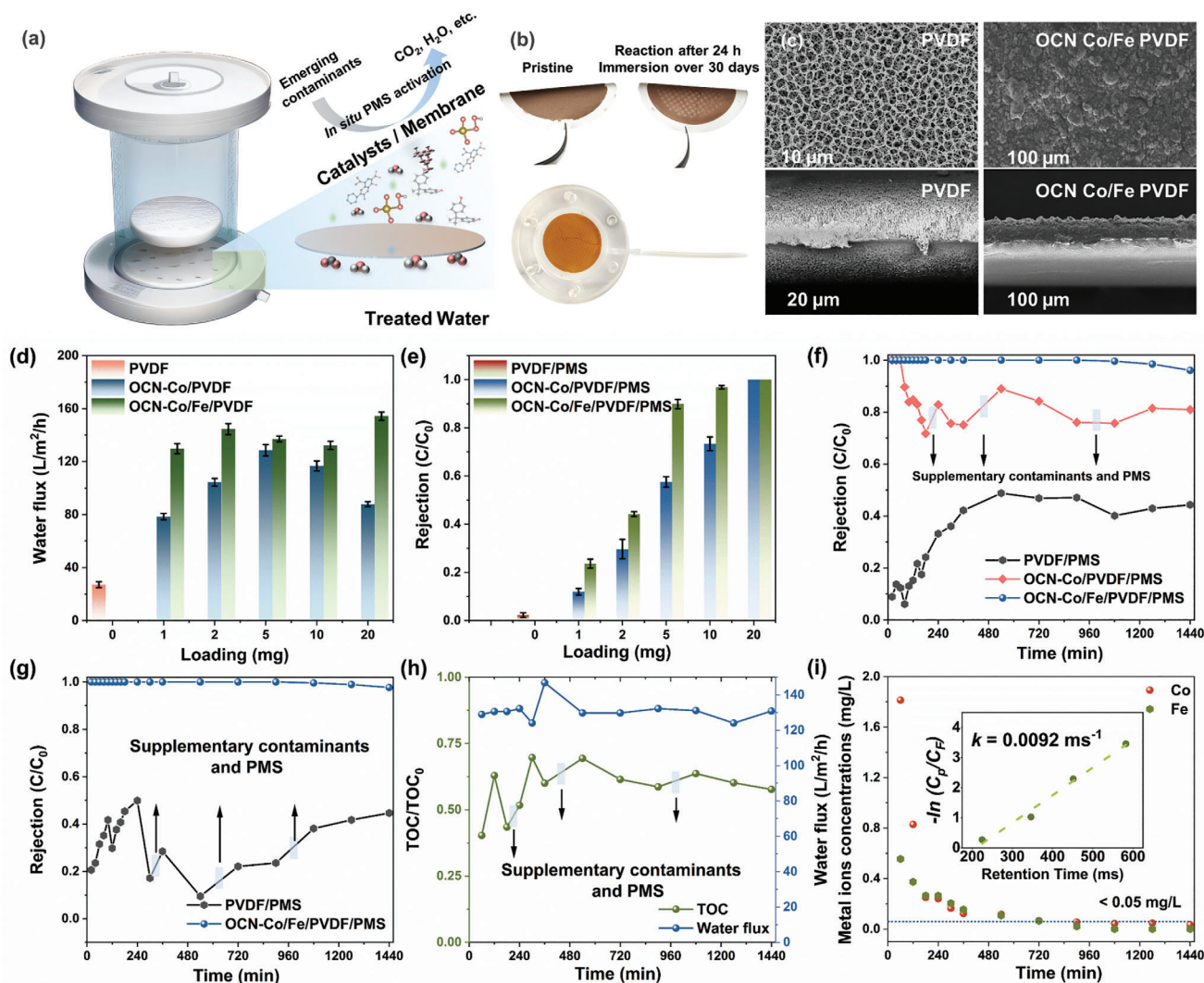
Figure 5. a) Schematic illustration of microreactor of PMS-based AOPs coupled with membrane filtration, b) photograph of the prepared OCN-Co/Fe membranes with an area of 12.56 cm² and the membrane exhibited high flexibility and stability, c) SEM images of PVDF and OCN-Co/Fe/PVDF surfaces and their cross-sectional scanning electron micrographs, d) water flux of OCN-Co/PVDF membranes and OCN-Co/Fe/PVDF membranes, e) CIP removal efficiency OCN-Co/PVDF membranes and OCN-Co/Fe/PVDF membrane, f) CIP rejection efficiency in effluent of PVDF membrane, OCN-Co/PVDF membrane and OCN-Co/Fe/PVDF membrane in micro-reactor as functions of filtration time, g) SMX removal efficiency in effluent of PVDF membrane, and OCN-Co/Fe/PVDF membrane in micro-reactor as functions of filtration time, h) water flux and TOC removal in effluent of OCN-Co/Fe/PVDF membranes in micro-reactor as functions of filtration time, i) cobalt and iron ions concentration in effluent of OCN-Co/Fe/PVDF in micro-reactor as functions of filtration time.

fabricated by self-assembling g-C_3N_4-based atom-site catalysts onto PVDF substrates through a vacuum filtration method (**Figure** 5a–c). A combination of peristaltic pumps and gravity was employed to facilitate the flow of pollutant solutions mixed with PMS through the membrane filtration microreactor. Following the incorporation of OCN-Co and OCN-Co/Fe, we observed a significant increase in both the water flux and catalytic performance of the composite membrane, as documented in Figure 5d. We controlled the thickness of composite membrane in terms of loading of catalysts, and systematically analyzed the correlation between the composite membrane's thickness, its pollutant removal efficiency, and water flux (Figures S36 and S37, Supporting Information). As shown in Figure 5e

and Table S8 (Supporting Information), OCN-Co/Fe/PVDF composite membrane exhibited stronger hydrophilicity, achieving 100% catalytic performance at a minimum membrane thickness of 24.3 μm, corresponding to the loading of 1.6 mg cm^{-2}, the flux of 154.29 L m^{-2} h^{-1} and the contacted angel of 18.38°. The excellent removal efficiency could be ascribed to uniform distributed dual metal active sites, thereby facilitating the rapid generation of active species that effectively decompose pollutants. Based on the retention time and removal efficiency, the first-order rate constant of OCN-Co/Fe/PVDF composite membrane for CIP reject efficiency was 33 min^{-1} (0.0092 ms^{-1}), which was 36.3 times than that of OCN-Co/Fe suspension (0.91 min^{-1}) (Figure 5i).

ADVANCED
SCIENCE NEWS

www.advancedsciencenews.com

ADVANCED
MATERIALS

www.advmat.de

The stability of OCN-Co/Fe/PVDF composite membrane (OCFM) and OCN-Co/PVDF composite membrane (OCM) were further evaluated by long-term flow reaction of 24 h. The rejection of CIP for OCFM maintained over 96% (over 24 h) at an average permeance of 130.95 L m^{-2} h^{-1}, which was superior than that of OCM and pristine membrane (above 75.07% and 6.11%, respectively) (Figure 5f). Moreover, OCFM also exhibited excellent catalytic performance for sulfamethoxazole removal (above 97.66% over 24 h) (Figure 5g). In the case of OCFM, cobalt ion concentrations in the treated water were measured at 35.4 ppm, while iron ion concentrations fell below the detection limit of inductively coupled plasma (ICP) analysis. (Figure 5i). Meanwhile, it was found that the total organic carbon removal in the effluent was more than 40.33% during the reaction (Figure 5h). Notably, the experiments also demonstrated the robustness of OCFM; no cracks, wrinkles, or color changes were observed following prolonged exposure to high flow rates and extended reaction times, suggesting its excellent oxidation ability and practicability.

3. Conclusion

This research offers analytical methods and design perspectives crucial for advancing catalytic membrane technologies based on g-C$_3$N$_4$-atom-site catalysts. Specifically, the interaction among synthesis, structure, and properties may be elucidated through controlled experimental designs, employing statistical tools such as correlation coefficients and the Mantel test. Due to strong interaction between support and isolated metal atoms, the introduction of O doping atoms into coordination environment could directly anchor metal atoms and result in blue shift of oxidation states, thus enhancing electron transfer rates of active sites and improving reaction rates. Catalytic efficiency can be further enhanced through the dual-metal orbital coupling effect, thus shifting the d band centers, promoting the electron transfer and reducing the antibonding states of key intermediates toward selective production of SO$_4^{\bullet-}$. Notably, a highly active, durability separation catalysis membrane loading OCN-Co/Fe catalysts was constructed. Fundamental understanding of the PMS activation mechanism with respect to heteroatom doping strategy and dual-atom coupling into one system will profound the design of catalysts with heightened activity and improved durability.

4. Experimental Section

Sample Preparation: OCN with co-doping of oxygen atoms and cyanide functional groups was synthesized using ball milling and calcination methods. A mixture of melamine (20 mmol, 2.52 g) and cyanuric acid (60 mmol, 7.74 g) was taken in a 100 mL ball milling jar. Subsequently, the mixture was ball-milled for 8 h in a ball mill at a speed of 240 rpm, alternating between clockwise rotation for 5 min and counterclockwise rotation for 5 min with 5 min of rest in between. The resulting mixture was calcined at 550 °C for 3 h with a heating rate of 2.3 °C min^{-1} in muffle furnace/tubular furnace. The solid products were washed with DI water six times and dried at 60 °C for 12 h. Bulk C$_3$N$_4$, OCN-Co, OCN-Fe, and OCN-Co/Fe were prepared by a direct pyrolysis of precursor or melamine under the same conditions. Table S1 (Supporting Information) is the assigned numbers and corresponding synthetic details for each catalyst.

Distance correlations between dissimilarities of synthetic conditions with the effect factors and catalytic performance of catalysts. Distances between samples on the basis of (i) synthetic conditions (Table S1, Supporting Information) and (ii) characterizations data and catalytic performance of catalysts (Tables S2–S4, Supporting Information) were computed pairwise. Based on distance matrices, partial Mantel correlations between synthetic conditions and characterizations data and catalytic performance of catalysts were performed using the vegan R software package.

EELS Mapping: The EELS spectra were acquired by K3 Cameras in Spectra 300 S/TEM operated at 300 kV. The convergence and collection angles were 19.6 and 8.47 mrad, respectively. The total exposure was 50 s under a controlled beam current at 100 pA.

Density Functional Theory Calculation: The structure geometries and electronic structure were optimized by spin-polarized DFT calculations via the Vienna Ab initio simulation package (VASP 6.3.2).[45] The generalized gradient approximation (GGA) method with the Perdew–Burke–Ernzerh (PBE) functional was used to treat the exchange-correlation interactions.[46] The projected augmented-wave method was applied to describe core electrons, and the valence electrons were described via the Kohn–Sham wave functions.[47] A 450 eV energy cutoff was adopted and the k-points in the Brillouin zone were sampled with $3 \times 3 \times 1$ by the Monkhorst–Pack scheme.[48] A 15 Å vacuum space was built to prohibit interactions between periodic units. All geometries were optimized when the residual force was lower than 0.02 eV Å^{-1}, and the energy convergence was set to 1×10^{-4} eV. The binding interactions between nitrogen-containing species and the catalyst were corrected by the DFT-D3 method.[49] The Crystal Orbital Hamilton Population (COHP) was calculated via the LOBSTER program in VASP.[50]

Supporting Information

Supporting Information is available from the Wiley Online Library or from the author.

Conflict of Interest

The authors declare no conflict of interest.

Data Availability Statement

The data that support the findings of this study are available in the supplementary material of this article.

[1] B. C. Hodges, E. L. Cates, J. H. Kim, *Nat. Nanotechnol.* **2018**, *13*, 642.

[2] a) J. Lee, U. von Gunten, J. H. Kim, *Environ. Sci. Technol.* **2020**, *54*, 3064; b) T. Liu, S. Xiao, N. Li, J. Chen, X. Zhou, Y. Qian, C.-H. Huang, Y. Zhang, *Nat. Commun.* **2023**, *14*, 2881.

[3] a) X. Liang, N. Fu, S. Yao, Z. Li, Y. Li, *J. Am. Chem. Soc.* **2022**, *144*, 18155; b) X.-Y. Ji, K. Sun, Z.-K. Liu, X. Liu, W. Dong, X. Zuo, R. Shao, J. Tao, *Nano-Micro Lett.* **2023**, *15*, 110.

[4] X. Li, X. Huang, S. Xi, S. Miao, J. Ding, W. Cai, S. Liu, X. Yang, H. Yang, J. Gao, J. Wang, Y. Huang, T. Zhang, B. Liu, *J. Am. Chem. Soc.* **2018**, *140*, 12469.

[5] a) S. An, G. Zhang, T. Wang, W. Zhang, K. Li, C. Song, J. T. Miller, S. Miao, J. Wang, X. Guo, *ACS Nano* **2018**, *12*, 9441; b) J. Xu, X. Zheng, Z. Feng, Z. Lu, Z. Zhang, W. Huang, Y. Li, D. Vuckovic, Y. Li, S. Dai, G. Chen, K. Wang, H. Wang, J. K. Chen, W. Mitch, Y. Cui, *Nat. Sustain.* **2021**, *4*, 233; c) L. S. Zhang, X. H. Jiang, Z. A. Zhong, L. Tian, Q. Sun, Y. T. Cui, X. Lu, J. P. Zou, S. L. Luo, *Angew. Chem., Int. Ed.* **2021**, *60*, 21751.

[6] J. Yang, W. Li, D. Wang, Y. Li, *Adv. Mater.* **2020**, *32*, 2003300.

[7] a) X. Zhou, M. Ke, G. Huang, C. Chen, W. Chen, K. Liang, Y. Qu, J. Yang, Y. Wang, F. Li, H. Yu, Y. Wu, *Proc. Natl. Acad. Sci. U. S. A.* **2022**, *119*, e2119492119; b) J. Song, N. Hou, X. Liu, M. Antonietti, P. Zhang, R. Ding, L. Song, Y. Wang, Y. Mu, *Adv. Mater.* **2023**, *35*, 2209552.

[8] Z. Wang, E. Almatrafi, H. Wang, H. Qin, W. Wang, L. Du, S. Chen, G. Zeng, P. Xu, *Angew. Chem., Int. Ed.* **2022**, *61*, e202202338.

[9] S. Chen, X. Li, C.-W. Kao, T. Luo, K. Chen, J. Fu, C. Ma, H. Li, M. Li, T.-S. Chan, M. Liu, *Angew. Chem., Int. Ed.* **2022**, *61*, e202206233.

[10] R. Li, D. Wang, *Adv. Energy Mater.* **2022**, *12*, 2103564.

[11] a) S. Lu, B. Huang, M. Sun, M. Luo, M. Jin, H. Yang, Q. Zhang, H. Liu, P. Zhou, Y. Chao, K. Yin, C. Shang, J. Wang, Y. Wang, F. Lv, L. Gu, S. Guo, *Nat. Synth.* **2023**, *3*, 576; b) X. Zhao, F. Wang, X. P. Kong, R. Fang, Y. Li, *J. Am. Chem. Soc.* **2021**, *143*, 16068.

[12] S. Zhang, M. Han, T. Shi, H. Zhang, Y. Lin, X. Zheng, L. R. Zheng, H. Zhou, C. Chen, Y. Zhang, G. Wang, H. Yin, H. Zhao, *Nat. Sustain.* **2022**, *6*, 169.

[13] a) R. Li, J. Zhao, B. Liu, D. Wang, *Adv. Mater.* **2024**, *36*, 2308653; b) X. Yi, H. Yang, X. Yang, X. Li, C. Yan, J. Zhang, L. Chen, J. Dong, J. Qin, G. Zhang, J. Wang, W. Li, Z. Zhou, G. Wu, X. Li, *Adv. Funct. Mater.* **2024**, *34*, 2309728; c) F. Liu, L. Shi, X. Lin, B. Zhang, Y. Long, F. Ye, R. Yan, R. Cheng, C. Hu, D. Liu, J. Qiu, L. Dai, *Sci Adv* **2023**, *9*, eadg0366.

[14] Y. Yang, X. Li, C. Zhou, W. Xiong, G. Zeng, D. Huang, C. Zhang, W. Wang, B. Song, X. Tang, X. Li, H. Guo, *Water Res.* **2020**, *184*, 116200.

[15] Y. Wang, J. Mao, X. Meng, L. Yu, D. Deng, X. Bao, *Chem. Rev.* **2019**, *119*, 1806.

[16] L. Han, H. Cheng, W. Liu, H. Li, P. Ou, R. Lin, H. T. Wang, C. W. Pao, A. R. Head, C. H. Wang, X. Tong, C. J. Sun, W. F. Pong, J. Luo, J. C. Zheng, H. L. Xin, *Nat. Mater.* **2022**, *21*, 681.

[17] a) G. Dong, G. Chen, B. Liu, L. J. Hounjet, Y. Cao, S. R. Stoyanov, M. Yang, B. Zhang, *Water Res.* **2022**, *211*, 118047; b) S. Zhang, T. Hedtke, Q. Zhu, M. Sun, S. Weon, Y. Zhao, E. Stavitski, M. Elimelech, J.-H. Kim, *Environ. Sci. Technol.* **2021**, *55*, 9266; c) M. Tian, Y. Liu, S. Zhang, C. Yu, K. Ostrikov, Z. Zhang, *Nat. Commun.* **2024**, *15*, 391.

[18] a) C. Li, J. Li, N. Huang, X. Y. Kong, Q. Xiao, Y. Huang, P. K. Wong, L. Ye, *npj Clean Water* **2023**, *6*, 47; b) C. Meng, B. Ding, S. Zhang, L. Cui, K. K. Ostrikov, Z. Huang, B. Yang, J. H. Kim, Z. Zhang, *Nat. Commun.* **2022**, *13*, 4010.

[19] a) Y. Gao, Y. Zhu, L. Lyu, Q. Zeng, X. Xing, C. Hu, *Environ. Sci. Technol.* **2018**, *52*, 14371; b) E. Jung, H. Shin, B. H. Lee, V. Efremov, S. Lee, H. S. Lee, J. Kim, W. Hooch Antink, S. Park, K. S. Lee, S. P. Cho, J. S. Yoo, Y. E. Sung, T. Hyeon, *Nat. Mater.* **2020**, *19*, 436; c) C. Tang, L. Chen, H. Li, L. Li, Y. Jiao, Y. Zheng, H. Xu, K. Davey, S. Z. Qiao, *J. Am. Chem. Soc.* **2021**, *143*, 7819.

[20] L. Chong, G. Gao, J. Wen, H. Li, H. Xu, Z. Green, J. D. Sugar, A. J. Kropf, W. Xu, X.-M. Lin, H. Xu, L.-W. Wang, D.-J. Liu, *Science* **2023**, *380*, 609.

[21] H. Yu, R. Shi, Y. Zhao, T. Bian, Y. Zhao, C. Zhou, G. I. N. Waterhouse, L. Z. Wu, C. H. Tung, T. Zhang, *Adv. Mater.* **2017**, *29*, 1605148.

[22] D. Zhao, C. Dong, B. Wang, C. Chen, Y. Huang, Z. Diao, S. Li, L. Guo, S. Shen, *Adv. Mater.* **2019**, *31*, 1903545.

[23] K. Chu, Q. Li, Y. Liu, J. Wang, Y. Cheng, *Appl. Catal. B* **2020**, *267*, 118693.

[24] M. A. Ahsan, A. R. Puente Santiago, Y. Hong, N. Zhang, M. Cano, E. Rodriguez-Castellon, L. Echegoyen, S. T. Sreenivasan, J. C. Noveron, *J. Am. Chem. Soc.* **2020**, *142*, 14688.

[25] a) Y. Li, H. Zhou, S. Cai, D. Prabhakaran, W. Niu, A. Large, G. Held, R. A. Taylor, X.-P. Wu, S. C. E. Tsang, *Nat. Catal.* **2024**, *7*, 77; b) L. Jian, G. Wang, X. Liu, H. Ma, *eScience* **2024**, *4*, 100206.

[26] a) C. Zhu, Y. Nie, S. Zhao, Z. Fan, F. Liu, A. Li, *Appl. Catal. B* **2022**, *305*, 121057; b) B. Zhang, C. Fang, J. Ning, R. Dai, Y. Liu, Q. Wu, F. Zhang, W. Zhang, S. Dou, X. Liu, *Carbon Neutralization* **2023**, *2*, 646.

[27] a) S. Sunagawa, L. P. Coelho, S. Chaffron, J. R. Kultima, K. Labadie, G. Salazar, B. Djahanschiri, G. Zeller, D. R. Mende, A. Alberti, F. M. Cornejo-Castillo, P. I. Costea, C. Cruaud, F. d'Ovidio, S. Engelen, I. Ferrera, J. M. Gasol, L. Guidi, F. Hildebrand, F. Kokoszka, C. Lepoivre, G. Lima-Mendez, J. Poulain, B. T. Poulos, M. Royo-Llonch, H. Sarmento, C. Vieira-Silva, C. Dimier, M. Picheral, S. Searson, et al., *Science* **2015**, *348*, 1261359; b) L. Wu, D. Ning, B. Zhang, Y. Li, P. Zhang, X. Shan, Q. Zhang, M. R. Brown, Z. Li, J. D. Van Nostrand, F. Ling, N. Xiao, Y. Zhang, J. Vierheilig, G. F. Wells, Y. Yang, Y. Deng, Q. Tu, A. Wang, D. Acevedo, M. Agullo-Barcelo, P. J. J. Alvarez, L. Alvarez-Cohen, G. L. Andersen, J. C. de Araujo, K. F. Boehnke, P. Bond, C. B. Bott, P. Bovio, R. K. Brewster, et al., *Nat. Microbiol.* **2019**, *4*, 1183.

[28] L. Cao, G. Luo, W. Liu, Y. Lin, X. Liu, Y. Cao, W. Zhang, Y. Wu, J. Yang, T. Yao, S. Wei, *Nat. Catal.* **2018**, *2*, 134.

[29] H. Wang, M. S. Bootharaju, J. H. Kim, Y. Wang, K. Wang, M. Zhao, R. Zhang, J. Xu, T. Hyeon, X. Wang, S. Song, H. Zhang, *J. Am. Chem. Soc.* **2023**, *145*, 2264.

[30] K. Sun, J. Dong, H. Sun, X. Wang, J. Fang, Z. Zhuang, S. Tian, X. Sun, *Nat. Catal.* **2023**, *6*, 1164.

[31] B. Wang, C. Cheng, M. Jin, J. He, H. Zhang, W. Ren, J. Li, D. Wang, Y. Li, *Angew. Chem., Int. Ed.* **2022**, *61*, e202207268.

[32] L. Wong, L. Huang, F. Zheng, Q. H. Thi, J. Zhao, Q. Deng, T. H. Ly, *Nat. Commun.* **2020**, *11*, 3982.

[33] F. Luo, A. Roy, L. Silvioli, D. A. Cullen, A. Zitolo, M. T. Sougrati, I. C. Oguz, T. Mineva, D. Teschner, S. Wagner, J. Wen, F. Dionigi, U. I. Kramm, J. Rossmeisl, F. Jaouen, P. Strasser, *Nat. Mater.* **2020**, *19*, 1215.

[34] C. H. Wu, C. Liu, D. Su, H. L. Xin, H.-T. Fang, B. Eren, S. Zhang, C. B. Murray, M. B. Salmeron, *Nat. Catal.* **2019**, *2*, 78.

[35] a) Y. Wei, J. Miao, P. J. J. Alvarez, M. Long, *Environ. Sci. Technol.* **2022**, *56*, 10557; b) J. Ning, B. Zhang, L. Siqin, G. Liu, Q. Wu, S. Xue, T. Shao, F. Zhang, W. Zhang, X. Liu, *Explor.* **2023**, *3*, 20230050.

[36] a) F. Qin, E. Almatrafi, C. Zhang, D. Huang, L. Tang, A. Duan, D. Qin, H. Luo, C. Zhou, G. Zeng, *Angew. Chem., Int. Ed.* **2023**, *62*, e202300256; b) N. Li, R. Li, X. Duan, B. Yan, W. Liu, Z. Cheng, G. Chen, L. a. Hou, S. Wang, *Environ. Sci. Technol.* **2021**, *55*, 16163.

[37] a) Q. Wu, Z. Yang, Z. Wang, W. Wang, *Proc. Natl. Acad. Sci. U. S. A.* **2023**, *120*, e2219923120; b) Y. Lei, Y. Yu, X. Lei, X. Liang, S. Cheng, G. Ouyang, X. Yang, *Environ. Sci. Technol.* **2023**, *57*, 5433.

[38] L. J. Yuan, B. Liu, L. X. Shen, Y. K. Dai, Q. Li, C. Liu, W. Gong, X. L. Sui, Z. B. Wang, *Adv. Mater.* **2023**, *35*, 2305945.

[39] Z. Guo, R. Sun, Z. Huang, X. Han, H. Wang, C. Chen, Y. Q. Liu, X. Zheng, W. Zhang, X. Hong, W. Li, *Proc. Natl. Acad. Sci. U. S. A.* **2023**, *120*, e2220608120.

[40] H. Xin, A. Vojvodic, J. Voss, J. K. Nørskov, F. Abild-Pedersen, *Phys. Rev. B* **2014**, *89*, 115114.

[41] a) Y. He, H. Qin, Z. Wang, H. Wang, Y. Zhu, C. Zhou, Y. Zeng, Y. Li, P. Xu, G. Zeng, *Appl. Catal. B* **2024**, *340*, 123204; b) H. Ma, F. Zhao,

ADVANCED
SCIENCE NEWS

www.advancedsciencenews.com

ADVANCED
MATERIALS

www.advmat.de

M. Li, P. Wang, Y. Fu, G. Wang, X. Liu, *Adv. Powder Mater.* **2023**, *2*, 100117.

[42] a) Y. Zong, X. Guan, J. Xu, Y. Feng, Y. Mao, L. Xu, H. Chu, D. Wu, *Environ. Sci. Technol.* **2020**, *54*, 16231; b) Y. Zong, H. Zhang, X. Zhang, W. Liu, L. Xu, D. Wu, *Appl. Catal. B* **2022**, *300*, 120722.

[43] X. Liu, Y. Jiao, Y. Zheng, M. Jaroniec, S.-Z. Qiao, *J. Am. Chem. Soc.* **2019**, *141*, 9664.

[44] Y. Zhou, E. Song, W. Chen, C. U. Segre, J. Zhou, Y. C. Lin, C. Zhu, R. Ma, P. Liu, S. Chu, T. Thomas, M. Yang, Q. Liu, K. Suenaga, Z. Liu, J. Liu, J. Wang, *Adv. Mater.* **2020**, *32*, 2003484.

[45] P. Grenier, D. Houde, S. Jandl, L. A. Boatner, *Phys. Rev. B* **1993**, *47*, 1.

[46] J. P. Perdew, K. Burke, M. Ernzerhof, *Phys. Rev. Lett.* **1996**, *77*, 3865.

[47] a) W. Kohn, L. J. Sham, *Phys. Rev.* **1965**, *140*, A1133; b) P. E. Blochl, *Phys. Rev B Condens. Matter* **1994**, *50*, 17953.

[48] H. J. Monkhorst, J. D. Pack, *Phys. Rev. B* **1976**, *13*, 5188.

[49] S. Grimme, J. Antony, S. Ehrlich, H. Krieg, *J. Chem. Phys.* **2010**, *132*, 154104.

[50] V. L. Deringer, A. L. Tchougréeff, R. Dronskowski, *J. Phys. Chem. A* **2011**, *115*, 5461.